Theoretical Study on Two-Dimensional Gaussian Rough Sea Surface Emission and Reflection in the Infrared Frequencies with Shadowing Effect

Christophe Bourlier, Gérard Berginc, and Joseph Saillard

***Abstract*—The emission and reflection properties of a two-dimensional (2-D) Gaussian rough sea surface are investigated. The emissivity and reflectivity study is of importance for accurate measurement of the temperature distribution of a wind-roughened water surface by infrared thermal imaging. The radius of curvature of the capillary waves being much larger than the wavelength involves the fact that our statistical model is based on the first order geometrical-optics method. In this paper, the first order geometrical optics approximation is considered because the higher order approximations can be neglected compared to the first order approximations. Indeed the total reflected electromagnetic field is damped by the multiple reflections on the surface. We introduce the 2-D shadowing function, and the observed surface length in the azimuthal direction with respect to the wind direction. Our emissivity and reflectivity model is obtained from recent works [1]–[3]. In order to use the 1-D (1-D) shadowing function [1], [2], assume that the average slope of the surface is smaller than unity. Assuming an infinite observed surface length as [1]–[3] determines only the emissivity with the 2-D shadowing function. Applying our emissivity and reflectivity model, the relation determining the apparent ocean surface temperature is given, in the considered wavelength band, according to the following parameters: wind speed, wavelength, polarization, intrinsic surface temperature, atmospheric transmission coefficient as evaluated by the Taylor and Larmor model [4], receiver location, and the camera field of view.**

***Index Terms*—Infrared remote sensing, ocean emissivity, reflectivity, rough surface, shadowing function.**

I. Introduction

REMOTE sensing of the Earth's environment by passive infrared sensing systems is important because it provides a tool in the study of weather forecasting, weather modification, pollution studies, and storm warning. These studies need a collection of environmental data over wide range of space within a limited time. In this paper, we discuss remote sensing of geophysical data in the ocean environment and the problems associated with passive infrared systems. In passive infrared equipment, the observing camera simply receives the natural radiation from the environment, such as the radiation from gas and aerosol, the radiation from the earth and the sun, and the radiation reflected by the earth. An example is thermal camera techniques. In an active system, the signal is sent out from the transmitter, interacts with the target or the clutter, and after the interaction this signal is observed and measured. Examples of active systems are lidar and radar.

Thermal emissions in the infrared bands can be used to probe the sea surface parameters: wave height and direction, surface temperature, foam distribution, and sea state. Passive thermal imaging of the ocean surface is currently measured from an aerial platform. If the platform is located near the sea surface, it becomes difficult to directly obtain the intrinsic radiation of the sea surface due to the fact that for grazing angles, the emissivity is of the same order as the hemispherical reflectivity. Therefore, we have to take into account the reflected sky background. In this case, it is interesting to compute the emissivity and reflectivity in order to determine the intrinsic sea-surface temperature from the emissivity knowledge by substracting the reflected sky background flux. In the case of high altitude observation, the observed zone may be considered infinite compared to the correlation length of the rough sea surface. For lower altitudes hundreds of meters to thousands of meters, the observed surface may become finite comparatively to the correlation length.

Contrary to the scattering problem in the microwave band, the first order geometrical-optics approximation can be used because the curvature radius of the capillary wave is much larger than the infrared wavelength. For microwave frequencies the emissivity is obtained by integrating the scattering coefficient over the half-space [5], where the scattering coefficient may be computed from the small perturbation method [5], [6]. Since shadowing effect is included, the multiple reflection can be neglected due to the fact that both phenomena are antagonist versus the incidence angle. Indeed, for grazing angles, the reflection number increases, whereas the illuminated surface decreases. We will verify this from simulations. In the microwave frequency band, the sea emissivity is lower than in infrared band, and the reflection coefficient on the sea surface is greater than for infrared wavelength [6], [7]. Consequently, the multiple reflection is noticeably larger in the microwave band.

In this paper, the theoretical study of the two-dimensional (2-D) rough sea surface emissivity and reflectivity is investigated in the infrared band in order to determine the apparent temperature of the sea surface. Our model is based on recent works [1]–[3]. Unlike [1], [2], the introduction of the 2-D shadowing function allows computation of the emissivity and reflectivity thoroughly, without the use of assumptions on the slope behaviors in the wind and crosswind directions. Assume an infinite observation length, as [1]–[3] computes only the emissivity

Manuscript received February 3, 2000; revised May 23, 2000.

C. Bourlier and J. Saillard are with Ecole Polytechnique de l'Université de Nantes, IRESTE, Nantes Cedex 3, France (e-mail: cbourlie@ireste.fr).

G. Berginc is with Thomson CSF Optronique, Guyancourt Cedex, France.

Publisher Item Identifier S 0196-2892(01)01199-8.

with the 2-D shadowing function. This paper quantified the size effect of the observed surface. In several articles, the emissivity have been modeled, but the sea surface is considered 1-D (1-D) [7]–[11], which involves that the wind direction not being introduced. Moreover, the shadowing effect is ignored.

Section II presents an extension of Smith's monostatic and bistatic 2-D shadowing functions [12] obtained from Smith's 1-D shadowing function [13], [14] by including the effect of the observation length. Smith's approach [14] is chosen because it is more accurate than Wagner's [15], as noted in [12]. In [12] the correlation between the slopes and the heights have been investigated on the average 2-D monostatic shadowing function. Since the difference between the correlated and uncorrelated results is small, the uncorrelated shadowing function is used. This allows to have a shadowing function simpler. For 2-D Gaussian surfaces, the monostatic shadowing function depends on the incidence angle θ on the slope variances in the wind and crosswind directions on the azimuthal direction ϕ according to the wind direction and on the new parameter, which is the normalized observation length y_0 to the length correlation with respect to ϕ. In the bistatic 2-D case, the shadowing function is expressed from $\{\theta_1, \phi_1, y_{01}, \theta_2, \phi_2, y_{02}\}$, which denote the incidence angles, the azimuthal directions according to the wind direction, and the normalized observation length with respect to ϕ_i of the transmitter and the receiver, respectively.

In Section III from the results of article [1]–[3], the 2-D emissivity, which is a monostatic magnitude and the reflectivity, which is a bistatic magnitude, are computed and simulated for a rough sea surface. According to the two-scale model [5], the capillary waves give the slope behavior provided by the Cox and Munk model [16], whereas the gravity waves are characterized by the height spatial autocorrelation function [17], giving the correlation length. Section IV presents the sea surface apparent temperature (SST) obtained from a radiative transfer method.

II. Shadowing Functions

The roughness of the sea surface involves that for grazing angles, a part of the sea surface is hidden. With the aim of quantify this phenomenon, the shadowing function is computed for the 1-D and 2-D stochastic surfaces, and in the monostatic (receiver and transmitter located as the same place) and the bistatic (distinct receiver and transmitter) cases. Theories of the analytical 1-D shadowing function have began with Bekman [18], Smith [13], [14] and Wagner [15], which are particular cases of Ricciardi–Sato's works [19], [20]. Indeed, Wagner's formulation retains only the first term of the Ricciardi–Sato's series, whereas Smith considers Wagner's approach by introducing a normalization function. Moreover the effect of the correlation is ignored, and the observation length is assumed to be infinite. Bourlier [12] explains in detail these different approaches and notes that Smith's results are better than Wagner's. Since the set of these approaches assumes an infinite surface, this section presents the monostatic and the bistatic 2-D shadowing functions [12] for a given observation length obtained from Smith's [13], [14] 1-D modeling.

A. 1-D Monostatic Shadowing Function

The Smith monostatic shadowing function S_m equal to the ratio of illuminated surface to the entire surface, is given by [13, (10)]

$$S_m(\theta, L_0, F) = \Upsilon(\mu - \gamma_0) \times \exp\left[-\int_0^{L_0} g(l)\, dl\right] \quad (1)$$

with θ the incidence angle L_0, the observation length $\mu = \cot\theta$, the slope of incident ray, and F, a point of the surface of height ξ_0, and slope γ_0. $\Upsilon(\mu - \gamma_0)$ is the unit step function defined as

$$\Upsilon(\mu - \gamma_0) = \begin{cases} 0 & \text{if } \gamma_0 \geq \mu \\ 1 & \text{else.} \end{cases} \quad (1a)$$

Contrary to article [13], a finite observation length L_0 is considered. For an uncorrelated Gaussian process the Smith function becomes [13]

$$g(l) = \frac{\mu}{\omega}\sqrt{\frac{2}{\pi}} \frac{\exp\left[-\left(\frac{\xi_0 + \mu l}{\omega\sqrt{2}}\right)^2\right]\Lambda(v)}{1 + \operatorname{erf}\left(\frac{\xi_0 + \mu l}{\omega\sqrt{2}}\right)} \quad (2)$$

with

$$\Lambda(v) = \frac{\exp(-v^2) - v\sqrt{\pi}\operatorname{erfc}(v)}{2v\sqrt{\pi}} \quad (2a)$$

and

$$v = \frac{\mu}{\sigma\sqrt{2}} = \frac{\cot\theta}{\sigma\sqrt{2}} \quad (2b)$$

with $\{\omega, \sigma\}$ the surface height and slope standard deviations, respectively. Substituting (2) into (1), the integration over l gives

$$S_m(\theta, L_0, F) = \Upsilon(\mu - \gamma_0) \times \left[\frac{1 - \frac{1}{2}\operatorname{erfc}\left(\frac{\xi_0}{\omega\sqrt{2}}\right)}{1 - \frac{1}{2}\operatorname{erfc}\left(\frac{\xi_0 + \mu L_0}{\omega\sqrt{2}}\right)}\right]^{\Lambda(v)} \quad (3)$$

where *erfc* denotes the complementary error function. When the observation length L_0 is infinite, (3) becomes [13, (22)]. For a Gaussian process, the average 1-D monostatic shadowing function $\overline{\overline{S}}_m$ over the heights ξ_0 and the slopes γ_0 is expressed as

$$\overline{\overline{S}}_m(\theta, L_0) = \frac{1}{2\pi\sigma\omega}\int_{-\infty}^{\infty}\int_{-\infty}^{\infty} S(\theta, F\{\xi_0, \gamma_0\}) \times \exp\left(-\frac{\xi_0^2}{2\omega^2} - \frac{\gamma_0^2}{2\sigma^2}\right) d\xi_0\, d\gamma_0 \quad (4)$$

and we show by using the variable transformation $h_0 = \xi_0/(\omega\sqrt{2})$ that

$$\overline{\overline{S}}_m(v, y_0) = \frac{1}{\sqrt{\pi}}\left[1 - \frac{1}{2}\operatorname{erfc}(v)\right]\int_{-\infty}^{\infty} \exp(-h_0^2) \times \left[\frac{1 - \frac{1}{2}\operatorname{erfc}(h_0)}{1 - \frac{1}{2}\operatorname{erfc}(h_0 + y_0 v)}\right]^{\Lambda(v)} dh_0 \quad (5)$$

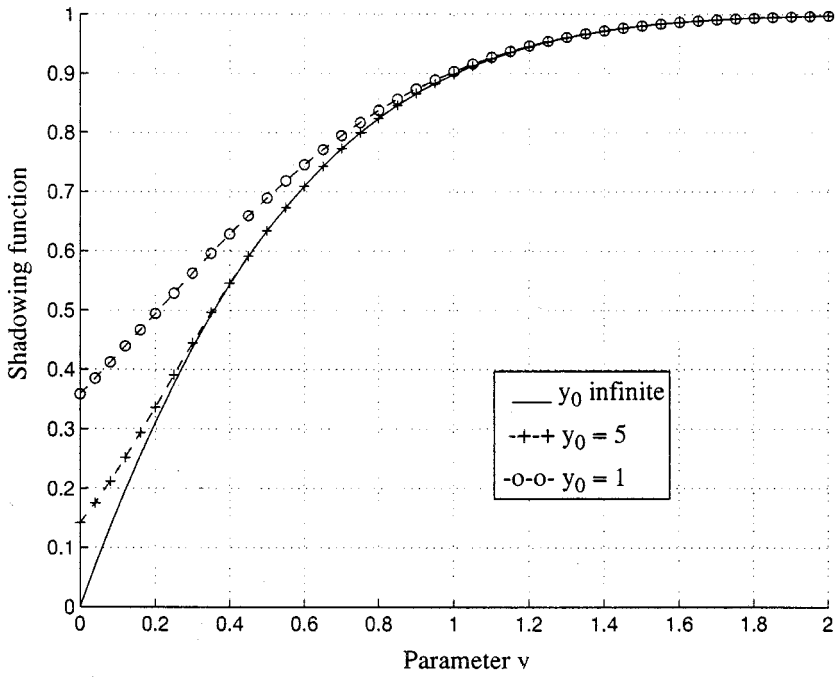

Fig. 1. One-dimensional (1-D) monostatic shadowing function versus v.

with

$$y_0 = \frac{L_0}{L_S} \qquad L_S = \frac{\omega}{\sigma} \tag{5a}$$

where y_0 is the normalized observation length with respect to the length L_S. For an infinite observation length, [13, (24)] is obtained.

As depicted in Fig. 1, for normal angles (v tends to 2) and for any y_0, the shadowing function converges to one due to the fact that the surface is entirely illuminated. For grazing angles (v tends to 0), the shadowing function becomes equal to zero when $y_0 \to \infty$, whereas it is not equal to zero when y_0 is small. For example, with $\{\theta = 80°;\ \sigma^2 = 0.4\}$, $v = 0.2$ [(2b)], and $S = \{0.3, 0.33, 0.50\}$ for $y_0 = \{\infty, 5, 1\}$, respectively. The reflectivity requires the knowledge of the bistatic shadowing function.

B. 1-D Bistatic Shadowing Function

For a stochastic process, the bistatic shadowing function represents the probability $S(\theta_1, \theta_2|F)$ that the incident ($y < 0$) and reflected ($y > 0$) rays of incidence angles $\{\theta_1, \theta_2\}$, respectively, are not crossed by the surface, knowing that they cross each other at the point F located on the surface with height ξ_0 and slope γ_0. For a given observation length, Wagner's formulation [15] leads to the following three cases:

$$S_m(\theta_1, \theta_2, F, L_0) = \begin{cases} S_1 = S_m(\theta_1, F, L_0) \times S_m(\theta_2, F, L_0) & \\ \qquad\qquad \text{for } \theta_2 \in [0;\ \pi/2] & \\ S_2 = S_m(\theta_1, F, L_0) \quad \text{for } \theta_2 \in [\theta_1;\ 0] & \\ S_3 = S_m(\theta_2, F, L_0) \quad \text{for } \theta_2 \in [-\pi/2;\ \theta_1[& \end{cases} \tag{6}$$

with $\theta_1 < 0$. Equation (6) indicates that the bistatic configuration is similar to two independent monostatic configurations. Using (3), the first case of (6) is written as

$$S_1 = \Pi_{[-|\mu_1|;\,\mu_2]} \times \left[\frac{1 - \frac{1}{2}\operatorname{erfc}\left(\frac{\xi_0}{\omega\sqrt{2}}\right)}{1 - \frac{1}{2}\operatorname{erfc}\left(\frac{\xi_0 + \mu_1 L_0}{\omega\sqrt{2}}\right)}\right]^{\Lambda(v_1)} \times \left[\frac{1 - \frac{1}{2}\operatorname{erfc}\left(\frac{\xi_0}{\omega\sqrt{2}}\right)}{1 - \frac{1}{2}\operatorname{erfc}\left(\frac{\xi_0 + \mu_2 L_0}{\omega\sqrt{2}}\right)}\right]^{\Lambda(v_2)} \tag{7}$$

with $\Pi_{[-|\mu_1|;\,\mu_2]} = \Upsilon(\mu_1 + \gamma_0)\Upsilon(\mu_2 - \gamma_0)$. Since the emitter is defined for $y < 0$, the sign of γ_0 in $\Upsilon(\mu_1 + \gamma_0)$ is positive, and

$$v = \frac{\cot|\theta_{1,2}|}{\sigma\sqrt{2}}. \tag{7a}$$

Substituting (7) into (4) and making the variable transformation $h_0 = \xi_0/(\omega\sqrt{2})$, the average bistatic shadowing function $\overline{\overline{S}}_1$ over the heights ξ_0 and the slopes γ_0 is expressed as

$$\overline{\overline{S}}_1(v_1, v_2, y_0) = \frac{1}{\sqrt{\pi}}\left\{1 - \frac{1}{2}[\operatorname{erfc}(v_1) + \operatorname{erfc}(v_2)]\right\} \times \int_{-\infty}^{\infty} \exp(-h_0^2) \times \left[\frac{1 - \frac{1}{2}\operatorname{erfc}(h_0)}{1 - \frac{1}{2}\operatorname{erfc}(h_0 + y_0 v_1)}\right]^{\Lambda(v_1)} \times \left[\frac{1 - \frac{1}{2}\operatorname{erfc}(h_0)}{1 - \frac{1}{2}\operatorname{erfc}(h_0 + y_0 v_2)}\right]^{\Lambda(v_2)} dh_0. \tag{8}$$

$\{v_{1,2}, \lambda\}$ are given by (7a) and (2a). The cases (a) and (b) being monostatics, we finally obtain

$$\overline{\overline{S}}_b(v_1, v_2, y_0) = \begin{cases} \overline{\overline{S}}_1, & \text{for } v_2 \in [0; \infty[\\ \overline{\overline{S}}_m(v_1, y_0), & \text{for } v_2 \in [-v_1; 0[\\ \overline{\overline{S}}_m(v_2, y_0), & \text{for } v_2 \in]-\infty; -v_1[\end{cases} \quad (9)$$

with $\overline{\overline{S}}_m$ given by (5). When the observation length is infinite, (9) becomes [12, 2.34].

Fig. 2 represents $\overline{\overline{S}}_b(v_1, v_2, y_0)$ as a function of v_2 for $y_0 = \{5, \infty\}$ and $v_1 = \{0.5, 1.5\}$. We observe that the shadowing function increases with $\{v_1, |v_2|\}$ and decreases with y_0. As in the monostatic case, the effect of the observation length is important for grazing angles corresponding to v_1 or $|v_2|$. Since the surface is 2-D, the monostatic and bistatic 2-D shadowing functions have to be determined for calculating the emissivity and reflectivity, respectively.

C. Two-Dimensional (2-D) Shadowing Function

We have seen that the 1-D monostatic shadowing function depends on the incidence angle θ, the slope standard deviation σ, and the normalized observation length y_0. In the 2-D case, the azimuthal direction ϕ must be introduced according to the wind direction (Fig. 3). Bourlier *et al.* [12] show that the 2-D shadowing function is obtained from that defined in the 1-D case by substituting in (2b) for the monostatic case, the surface slope variance σ^2 by the surface slope variance σ_X^2 expressed in the $(0X)$ direction characterized by the azimuthal direction ϕ. For the bistatic case in (7a), σ^2 is substituted by $\sigma_{X_{1,2}}^2$ defined according to the azimuthal directions $\{\phi_1, \phi_2\}$ of the transmitter and receiver. We have

$$\sigma_{X_{1,2}}^2 = \alpha + \beta \times \cos(2\phi_{1,2}) \quad (10)$$

with

$$\alpha = \frac{\sigma_x^2 + \sigma_y^2}{2}, \qquad \beta = \frac{\sigma_x^2 - \sigma_y^2}{2} \quad (11)$$

where $\{\sigma_x^2, \sigma_y^2\}$ are the surface slope variances in the wind $(0x)$ and crosswind $(0y)$ directions, respectively. This involves, from (5a), that the length L_S in the monostatic case becomes

$$y_0 = \frac{L_0}{L_S} \qquad L_S = \frac{\omega}{\sigma_X} \quad (12)$$

and $L_{S_{1,2}}$ in the bistatic configuration is

$$y_{0_{1,2}} = \frac{L_0}{L_{S_{1,2}}} \qquad L_{S_{1,2}} = \frac{\omega}{\sigma_{X_{1,2}}}. \quad (13)$$

Fig. 4 depicts the 2-D monostatic shadowing function as a function of the azimuthal direction ϕ according to the wind direction for different incidence angles $\theta = \{75, 80, 85, 88, 89\}^o$ and with a normalized observation length $y_o = \{5, \text{infinite}\}$. The slope $\{\sigma_x^2, \sigma_y^2\}$ variances are obtained from the Cox and Munk model [16]

$$\sigma_x^2 = 3.16 \times 10^{-3} u_{12} \qquad \sigma_y^2 = 0.003 + 1.92 \times 10^{-3} u_{12} \quad (14)$$

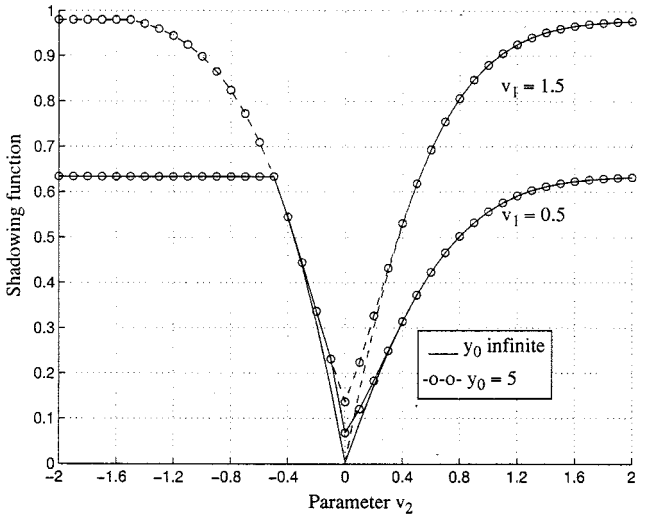

Fig. 2. Two-dimensional (2-D) bistatic shadowing function versus v_2.

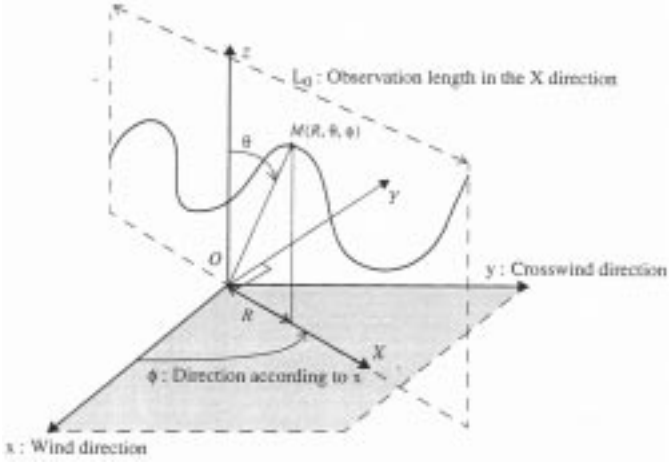

Fig. 3. Definition of the two-dimensional (2-D) monostatic shadowing function.

with a wind speed u_{12} defined at 12.5 m above the sea equal to 10.3 m/s. We observe in Fig. 4 that the shadowing function varies slightly with the direction ϕ and decreases with the incidence angle θ. Since the normalized observation length decreases, the illuminated surface increases for grazing angles.

Fig. 5 plots the 2-D shadowing function of an infinite surface ($y_0 = \infty$) with respect to the incidence angle θ_2 with $\phi = \phi_1 = \phi_2 = \{0, 45, 90\}^o$, $|\theta_1| = \{75, 80, 85\}^o$, and $u_{12} = 10.3$ m/s.

III. Emissivity and Reflectivity

The emissivity is a pertinent parameter for evaluating the sea surface temperature (SST). In most SST retrieval algorithms, the sea surface emissivity has been assumed, explicitly or implicitly, to be a constant (e.g., 0.98). This assumption is verified for normal incidence angles smaller than 30° and it may be used for a camera located on a satellite platform. But for infrared systems at low altitude, i.e., for angles greater than 60°, the emissivity depends on the incidence angle θ and on the azimuthal direction ϕ according to the wind direction. Moreover, the reflected radiation by the surface is of the same order as the one radiated by the surface, which involves that the reflectivity also must be

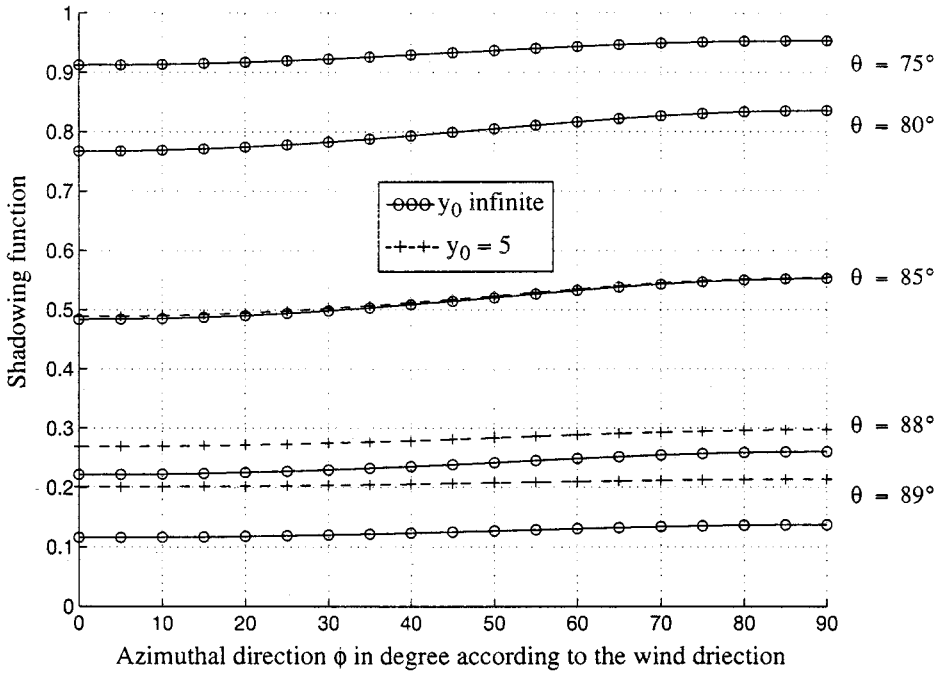

Fig. 4. Two-dimensional (2-D) monostatic shadowing function with respect to the azimuthal direction ϕ according to the wind direction.

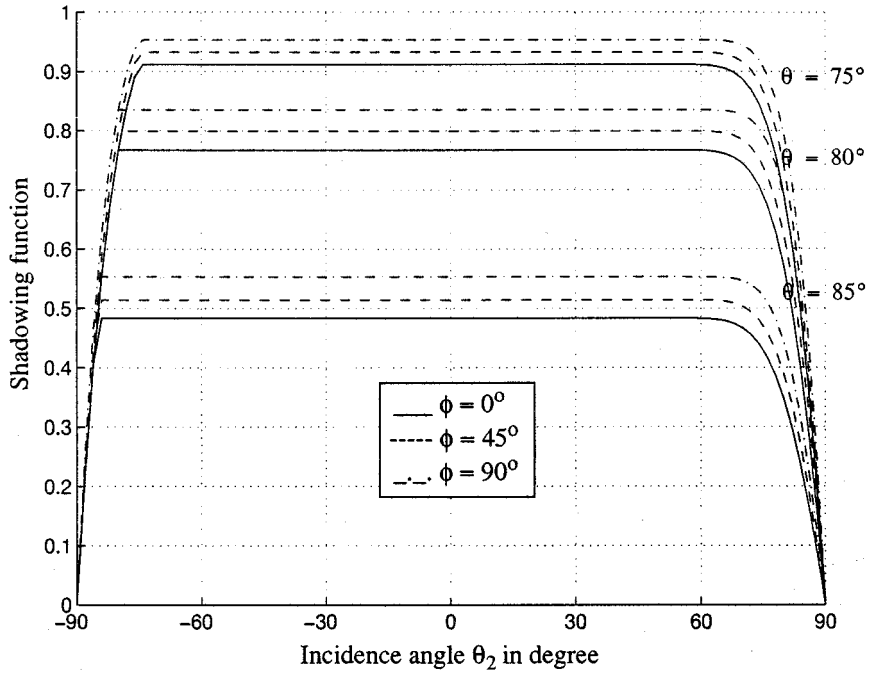

Fig. 5. Two-dimensional (2-D) monostatic shadowing function with respect to the incidence angle θ_2 with $\theta = \theta_1 = \theta_2$ for an infinite surface.

determined, in order to substract this signal, for computing the infrared intrinsic radiation from the sea surface.

Emissivity models developed by Watts–Allen–Nightingale [7], Masuda–Takashima–Takayama [8], Saunders [9], Wu–Smith [10], Zeisse–McGrath–Littfin [11] neglect the dependence of the direction ϕ, and the shadowing effect is ignored. Our model is based on the works of Yoshimori–Itoh–Ichioka [2] and Bourlier *et al.* [3]. Unlike [2], in the introduction of the 2-D shadowing function, no assumption is made on the slopes variances. Indeed, in order to use the 1-D shadowing function, Yoshimori [2] neglects the cross-wind slope γ_y^2 in comparison with $1 + \gamma_x^2$, with γ_x^2 the wind slope, and assumes that the observed surface is infinite. Bourlier [3] includes only the 2-D shadowing function of the emissivity determination, assuming that the observed surface is infinite.

The two-scale model is commonly used for representing the sea surface [5]. The small scale gives the capillary waves behavior, whereas the large scale corresponds to the gravity waves. The ocean surface is obtained from the superposition of these two scales. The capillary waves have a radius of curvature R_C

on the order of millimeters, which is much larger than the wavelength λ in the visible and infrared range. This involves that each facet can be regarded as flat with respect to the radiation, and the interaction of the sea surface with light can be treated with geometric optics. For example, in the 1-D case, the mathematical criteria is expressed as [10]

$$2\pi R_C \cos^3(\theta) \gg \lambda \tag{15}$$

and for a Gaussian autocorrelation function, the radius of curvature [5] is

$$R_C = \frac{\omega}{\sigma^2}\sqrt{\frac{\pi}{6}} = 0.724\frac{\omega}{\sigma^2}. \tag{16}$$

Consequently, for a slope standard deviation σ lower than unity and for a height standard deviation larger than a millimeter, the criteria (15) is valid in the infrared band.

A. Emissivity

From the approach developed by Yoshimori [1], [2], Bourlier [3] showed that the 2-D emissivity with respect to the wind direction ϕ with a Gaussian process and for an infinite observation length is expressed as

$$\varepsilon(\theta,\,\phi) = \frac{1}{2\pi\sqrt{\alpha^2+\beta^2}}\int_{-\infty}^{\infty}\int_{-\infty}^{\infty}[1-|r(|\varphi|)|^2] \times \exp(-a\gamma_Y^2 - 2b\gamma_X\gamma_Y - c\gamma_X^2)\times g\times \overline{S}_m\, d\gamma_X\, d\gamma_Y \tag{17}$$

with

$$\begin{cases} \cos\varphi = \dfrac{\cos\theta - \gamma_X\sin\theta}{\sqrt{1+\gamma_X^2+\gamma_Y^2}} & g = 1-\gamma_X\tan\theta \\ a = \dfrac{\alpha+\beta\cos(2\phi)}{2(\alpha^2-\beta^2)} & b = \dfrac{\beta\sin(2\phi)}{2(\alpha^2-\beta^2)} \\ c = \dfrac{\alpha-\beta\cos(2\phi)}{2(\alpha^2-\beta^2)} \end{cases} \tag{17a}$$

where $\{\gamma_X,\,\gamma_Y\}$ are the slopes of the surface in the $(0X)$ and orthogonal (OY) directions. $\{\alpha,\,\beta\}$ are given by (11). r are Fresnel's coefficients either in vertical polarization V (electromagnetic field parallel to the incidence plane) or in horizontal polarization (electromagnetic field orthogonal to the incidence plane) given by

$$\begin{cases} r_V(\varphi) = \dfrac{n\cos\varphi - \cos\varphi'}{n\cos\varphi + \cos\varphi'} \\ r_H(\varphi) = \dfrac{\cos\varphi - n\cos\varphi'}{\cos\varphi + n\cos\varphi'} \end{cases} \quad \text{with } \sin\varphi' = \frac{\sin\varphi}{n} \tag{18}$$

where n is the refractive index of the sea water, and ϕ' denotes the refraction angle given by Snell–Descartes's law. The air refractive index is assumed to be equal to one. $\overline{S}_m$ denotes the 2-D monostatic shadowing function integrated over the height ξ_0. Contrary to [3], a finite observation length L_0 is considered, and we have shown that

$$\overline{S}_m(\theta,\,\phi,\,\gamma_X) = \frac{\Upsilon(\cot\theta-\gamma_X)}{\sqrt{\pi}}\int_{-\infty}^{\infty}\exp(-h_0^2) \times\left[\frac{1-\frac{1}{2}\operatorname{erfc}(h_0)}{1-\frac{1}{2}\operatorname{erfc}(h_0+y_0 v)}\right]^{\Lambda(v)} dh_0. \tag{19}$$

As the integration over γ_X is not computed, the term $1-\operatorname{erfc}(v)/2$ is replaced by $\Upsilon(\cot\theta-\gamma_X)$ in (5). The substitution of (19) into (17) leads to

$$\varepsilon(\theta,\,\phi) = \frac{1}{2\pi\sqrt{\pi}\sqrt{\alpha^2+\beta^2}} \times\int_{-\infty}^{\infty}\left\{\int_{-\infty}^{\cot\theta}[1-|r(|\varphi|)|^2] \times\exp(-a\gamma_Y^2 - 2b\gamma_X\gamma_Y - c\gamma_X^2) \times(1-\gamma_X\tan\theta)\,d\gamma_X\right\} d\gamma_Y \times\int_{-\infty}^{\infty}\exp(-h_0^2)\times\left[\frac{1-\frac{1}{2}\operatorname{erfc}(h_0)}{1-\frac{1}{2}\operatorname{erfc}(h_0+y_0 v)}\right]^{\Lambda(v)} dh_0. \tag{20}$$

Therefore, the calculation of average emissivity requires two linked integrations over the $\{\gamma_X,\,\gamma_Y\}$ and an independent integration over the height ξ_0. For an infinite observation length $y_0 \to \infty$, (20) becomes [3, (3.21)].

B. Mathematical Development of the Reflectivity

Let O be a point of the surface defining the origin of Cartesian coordinates $(x,\,y,\,z)$ (Fig. 6), $\vec{n}$ the unitary vector in the direction z, $\vec{n}$ the unitary vector normal to the facet, and $\{\vec{s}_1,\,\vec{s}_2\}$ the unitary vectors of observation directions of the transmitter and receiver, respectively. These vectors in polar coordinates are defined as

$$\vec{n} = \begin{bmatrix}0\\0\\1\end{bmatrix} \qquad \vec{n}' = \frac{1}{\sqrt{1+\gamma_x^2+\gamma_y^2}}\begin{bmatrix}-\gamma_x\\-\gamma_y\\1\end{bmatrix}$$

$$\vec{s}_1 = \begin{bmatrix}s_{1x}=\sin\theta_1\cos\phi_1\\ s_{1y}=\sin\theta_1\sin\phi_1\\ s_{1z}=\cos\theta_1\end{bmatrix}$$

$$\vec{s}_2 = \begin{bmatrix}s_{2x}=\sin\theta_2\cos\phi_2\\ s_{2y}=\sin\theta_2\sin\phi_2\\ s_{2z}=\cos\theta_2\end{bmatrix} \tag{21}$$

where

- $\{\gamma_x,\,\gamma_y\}$ surface slopes in the wind and crosswind directions;
- $\{\theta_1,\,\theta_2\}$ incidence angles of the transmitter and receiver, respectively;
- $\{\phi_1,\,\phi_2\}$ azimuthal directions according to the wind direction (Ox).

The reflectivity w for a Gaussian surface is expressed as [2]

$$w = \frac{1}{2\pi\sigma_x\sigma_y}\int_{-\infty}^{\infty}\int_{-\infty}^{\infty}\delta(\theta-\theta_1)\times\delta(\phi-\phi_1)\times g\times\overline{S}_b \times\exp\left(-\frac{\gamma_x^2}{2\sigma_x^2}-\frac{\gamma_y^2}{2\sigma_y^2}\right) d\gamma_x\,d\gamma_y \tag{22}$$

where g is given by

$$g = \frac{\vec{n}'\cdot\vec{s}}{(\vec{n}\cdot\vec{n}')(\vec{n}\cdot\vec{s})} = 1-(\gamma_x\cos\phi_2+\gamma_y\sin\phi_2)\times\tan\theta_2. \tag{22a}$$

r are (18) Fresnel's coefficients, $\overline{S}_b$ is the 2-D bistatic shadowing function integrated over the height ξ_0, δ is the Dirac distribution, and $\varphi = (\vec{n}', \vec{s}_2)$. Contrary to the determination of the emissivity, the integrations over the slopes $\{\gamma_x, \gamma_y\}$ are not required due to the fact that there is a uniqueness of $\{\gamma_{x0}, \gamma_{y0}\}$ that gives the specular direction when $\{\theta = \theta_1, \phi = \phi_1\}$ in the double integrations (22). We propose to find this set. The specular reflection is expressed as

$$\vec{s}_1 = 2 \times (\vec{n}' \cdot \vec{s}_2) \cdot \vec{n}' - \vec{s}_2 = 2 \times \cos(\varphi) \times \vec{n}' - \vec{s}_2 \quad (23)$$

with

$$\cos\,\varphi = \vec{n}' \cdot \vec{s}_2 = \frac{\cos\,\theta_2 - \sin\,\theta_2(\gamma_x\,\cos\,\phi_2 + \gamma_y\,\sin\,\phi_2)}{\sqrt{1+\gamma_x^2+\gamma_y^2}}. \quad (23a)$$

Hence

$$\vec{s}_1 = \begin{bmatrix} s_{1x} = -\left(\dfrac{2\gamma_x\,\cos\,\varphi}{\sqrt{1+\gamma_x^2+\gamma_y^2}} + \sin\,\theta_2\,\cos\,\phi_2\right) \\ s_{1y} = -\left(\dfrac{2\gamma_y\,\cos\,\varphi}{\sqrt{1+\gamma_x^2+\gamma_y^2}} + \sin\,\theta_2\,\sin\,\phi_2\right) \\ s_{1z} = \dfrac{2\,\cos\,\varphi}{\sqrt{1+\gamma_x^2+\gamma_y^2}} + \cos\,\theta_2 \end{bmatrix}. \quad (23b)$$

Substituting (23a) and (23b) into (21), the angles $\{\theta_1, \phi_1\}$ are

$$\begin{cases} \cos\,\theta_1 = s_{1z} = \dfrac{2[\cos\,\theta_2 - \sin\,\theta_2(\gamma_x\,\cos\,\phi_2 + \gamma_y\,\sin\,\phi_2)]}{1+\gamma_x^2+\gamma_y^2} \\ \qquad\qquad - \cos\,\theta_2 \\ \tan\,\phi_1 = \dfrac{s_{1y}}{s_{1x}} = \dfrac{\gamma_y(\cos\,\theta_1 + \cos\,\theta_2) + \sin\,\theta_2\,\sin\,\phi_2}{\gamma_x(\cos\,\theta_1 + \cos\,\theta_2) + \sin\,\theta_2\,\cos\,\phi_2}. \end{cases} \quad (24)$$

The integral (22) is not equal to zero when $\{\theta = \theta_1, \phi = \phi_1\}$, we have to calculate the values of $\{\gamma_{x0}, \gamma_{y0}\}$ which verified (24), i.e., to resolve the equations system of two variables $\{\gamma_x, \gamma_y\}$, and we show that the component γ_{x0} verifies the solution of the following equation of second degree

$$\gamma_{x0}^2 \times s_z^3 + 2\gamma_{x0} \times s_z^2 s_{2x} + s_z(s_{2x}^2 - s_{1x}^2) = 0 \quad (25)$$

with

$$s_z = \cos\,\theta_1 + \cos\,\theta_2 \quad (25a)$$

where the solutions are

$$\gamma_{x0} = -\frac{s_{2x} \pm |s_{1x}|}{s_{1z} + s_{2z}}. \quad (26)$$

Substituting (26) into (24), the slope in the cross-wind direction is given by

$$\gamma_{y0} = -\frac{s_{2y} \pm |s_{1y}|}{s_{1z} + s_{2z}}. \quad (27)$$

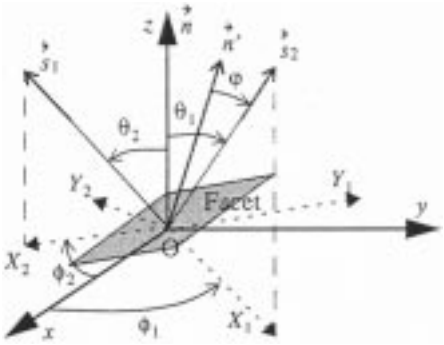

Fig. 6. Reflectivity of a facet.

For a plane, i.e., $\{\gamma_{x0}, \gamma_{y0}\} = 0$, the specular reflection is obtained from $\theta_2 = -\theta_1$ and $\phi_2 = \phi_1$, which involves

$$\gamma_{x0} = -\frac{s_{2x} + s_{1x}}{s_{1z} + s_{2z}} \qquad \gamma_{y0} = -\frac{s_{2y} + s_{1y}}{s_{1z} + s_{2z}} \quad (28)$$

with

$$\theta_1 \in [-\pi/2; \pi/2] \qquad \phi_1 \in [0; \pi]. \quad (28a)$$

Hence, integral (22) is written as

$$\begin{aligned} w(\theta_1, \phi_1, \theta_2, \phi_2) &= \frac{1}{2\pi\sigma_x\sigma_y}\,\exp\left(-\frac{\gamma_{x0}^2}{2\sigma_x^2} - \frac{\gamma_{y0}^2}{2\sigma_y^2}\right) \\ &\quad \times |r(|\varphi(\theta_2, \phi_2, \gamma_{x0}, \gamma_{y0})|)|^2 \\ &\quad \times g(\theta_2, \phi_2, \gamma_{x0}, \gamma_{y0}) \times \overline{S}_b(\theta_1, \phi_1, \theta_2, \phi_2, \gamma_{x0}, \gamma_{y0}) \end{aligned} \quad (29)$$

where φ and g are obtained by substituting (28) into (23a) and (22a)

$$\begin{cases} \cos\,\varphi|_{\gamma_{x0}, \gamma_{y0}} \\ \quad = \sqrt{\dfrac{1 + \cos\,\theta_1\,\cos\,\theta_2 + \sin\,\theta_1\,\sin\,\theta_2\,\cos(\phi_2 - \phi_1)}{2}} \\ g|_{\gamma_{x0}, \gamma_{y0}} = \dfrac{1 + \cos\,\theta_1\,\cos\,\theta_2 + \sin\,\theta_1\,\sin\,\theta_2\,\cos(\phi_2 - \phi_1)}{\cos\,\theta_2(\cos\,\theta_1 + \cos\,\theta_2)}. \end{cases} \quad (29a)$$

J is the Jacobian introduced by the variable transformations equal to

$$\begin{aligned} J &= \left|\frac{\partial\gamma_{x0}}{\partial\theta_1}\,\frac{\partial\gamma_{y0}}{\partial\phi_1} + \frac{\partial\gamma_{x0}}{\partial\phi_1}\,\frac{\partial\gamma_{y0}}{\partial\theta_1}\right| \\ &= \left|\frac{\sin\,\theta_1[1 + \cos\,\theta_1\,\cos\,\theta_2 + \sin\,\theta_1\,\sin\,\theta_2\,\cos\,(\phi_2 - \phi_1)]}{(\cos\,\theta_1 + \cos\,\theta_2)^3}\right|. \end{aligned} \quad (29b)$$

The reflectivity depends then on $\{\theta_1, \phi_1, \theta_2, \phi_2, \sigma_x,$ and $\sigma_y\}$. We have proved that the 2-D bistatic shadowing functions $\overline{S}_b(\theta_1, \phi_1, \theta_2, \phi_2, \sigma_x, \sigma_y)$ integrated over the height ξ_0 is

$$\overline{S}_b(\theta_1, \phi_1, \theta_2, \phi_2, \sigma_x, \sigma_y) = \begin{cases} \overline{S}_1 & \text{for } \theta_2 \in [0; \pi/2] \\ \overline{S}_2 & \text{for } \theta_2 \in [|\theta_1|; 0] \\ \overline{S}_3 & \text{for } \theta_2 \in [-\pi/2; -|\theta_1|[\end{cases} \quad (30)$$

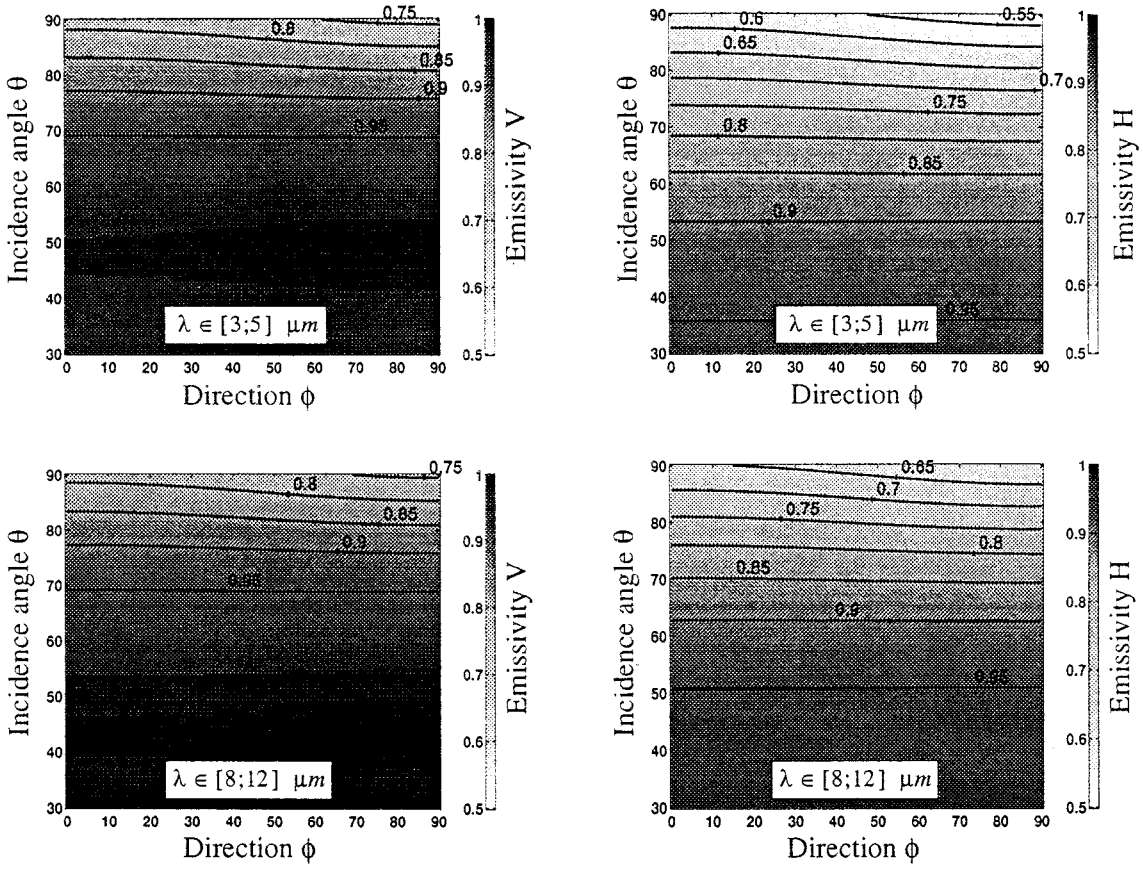

Fig. 7. Average emissivity on $\lambda \in [3;5]\ \mu$m and $\lambda \in [8;12]\ \mu$m versus the azimuthal direction ϕ according to the wind direction and the incidence angle θ in V and H polarizations with $u_{12} = 10.3$ m/s for an infinite surface.

with

$$\overline{S}_1 = \begin{cases} \dfrac{1}{\sqrt{\pi}} \displaystyle\int_{-\infty}^{\infty} \exp(-h_0^2) \\ \times \left[\dfrac{1 - \frac{1}{2}\operatorname{erfc}(h_0)}{1 - \frac{1}{2}\operatorname{erfc}(h_0 + y_0 v_1)} \right]^{\Lambda(v_1)} \\ \times \left[\dfrac{1 - \frac{1}{2}\operatorname{erfc}(h_0)}{1 - \frac{1}{2}\operatorname{erfc}(h_0 + y_0 v_2)} \right]^{\Lambda(v_2)} dh_0 \\ \quad \text{if } \begin{cases} \gamma_{X_1 0} \in [-|\mu_1|; 0] \\ \gamma_{X_2 0} \in [0; \mu_2] \end{cases} \\ \quad \text{else } 0 \end{cases} \tag{30a}$$

$$\overline{S}_2 = \begin{cases} \dfrac{1}{\sqrt{\pi}} \displaystyle\int_{-\infty}^{\infty} \exp(-h_0^2) \\ \times \left[\dfrac{1 - \frac{1}{2}\operatorname{erfc}(h_0)}{1 - \frac{1}{2}\operatorname{erfc}(h_0 + y_0 v_2)} \right]^{\Lambda(v_2)} dh_0 \\ \quad \text{if } \gamma_{X_2 0} \le \mu_2 \\ \quad \text{else } 0 \end{cases} \tag{30b}$$

$$\overline{S}_3 = \begin{cases} \dfrac{1}{\sqrt{\pi}} \displaystyle\int_{-\infty}^{\infty} \exp(-h_0^2) \\ \times \left[\dfrac{1 - \frac{1}{2}\operatorname{erfc}(h_0)}{1 - \frac{1}{2}\operatorname{erfc}(h_0 + y_0 v_1)} \right]^{\Lambda(v_1)} dh_0 \\ \quad \text{if } \gamma_{X_2 0} - |\mu_1| \\ \quad \text{else } 0 \end{cases} \tag{30c}$$

TABLE I

	$\lambda \in [3;5]\ \mu$			$\lambda \in [8;12]\ \mu$		
	$\varepsilon_i(0,0)$	$\varepsilon_i(90,90)$	$\Delta\varepsilon_i$	$\varepsilon_i(0,0)$	$\varepsilon_i(90,90)$	$\Delta\varepsilon_i$
u_{12} = 6.0 m/s	V : 0.996 H : 0.973	V : 0.666 H : 0.456	V : 0.330 H : 0.517	V : 0.998 H : 0.988	V : 0.672 H : 0.533	V : 0.326 H : 0.455
u_{12} = 10.3 m/s	V : 0.994 H : 0.972	V : 0.739 H : 0.527	V : 0.255 H : 0.445	V : 0.997 H : 0.987	V : 0.744 H : 0.606	V : 0.253 H : 0.381
u_{12} = 13.9 m/s	V : 0.993 H : 0.971	V : 0.776 H : 0.567	V : 0.216 H : 0.404	V : 0.996 H : 0.987	V : 0.780 H : 0.646	V : 0.216 H : 0.341

where $\{v_1, v_2\}$ are given by (7a) with $\sigma = \sigma_{X_{1,2}}$ (10), and $y_{0_{1,2}} = L_0/L_S$ defined from (13), which are the normalized observation lengths in the $\{\phi_1, \phi_2\}$ azimuthal directions, respectively. Since the integration over the slopes is not calculated, the terms *erfc* in (9) are replaced by the conditions in $\{\gamma_{X_1 0}, \gamma_{X_2 0}\}$ corresponding to the $\Upsilon(\mu_1+\gamma_{X_1 0})\Upsilon(\mu_2-\gamma_{X_2 0})$, $\Upsilon(\mu_2-\gamma_{X_2 0})$, $\Upsilon(\mu_1+\gamma_{X_1 0})\}$ functions, respectively. $\{\gamma_{X_1 0}, \gamma_{X_2 0}\}$ denotes the surface slopes defined in the transmitter (OX_1) and receiver (OX_2) directions (Fig. 6)

$$\begin{cases} \gamma_{X_1 0} = \gamma_{x0}\cos\phi_1 + \gamma_{y0}\sin\phi_1 \\ \qquad = -\dfrac{\sin\theta_1 + \sin\theta_2\cos(\phi_2 - \phi_1)}{\cos\theta_1 + \cos\theta_2} \\ \gamma_{X_2 0} = \gamma_{x0}\cos\phi_2 + \gamma_{y0}\sin\phi_2 \\ \qquad = -\dfrac{\sin\theta_2 + \sin\theta_1\cos(\phi_2 - \phi_1)}{\cos\theta_1 + \cos\theta_2}. \end{cases} \tag{31}$$

C. Simulations

In this paragraph, the emissivity and the reflectivity of a 2-D sea surface is simulated. They depend on Fresnel's coefficients

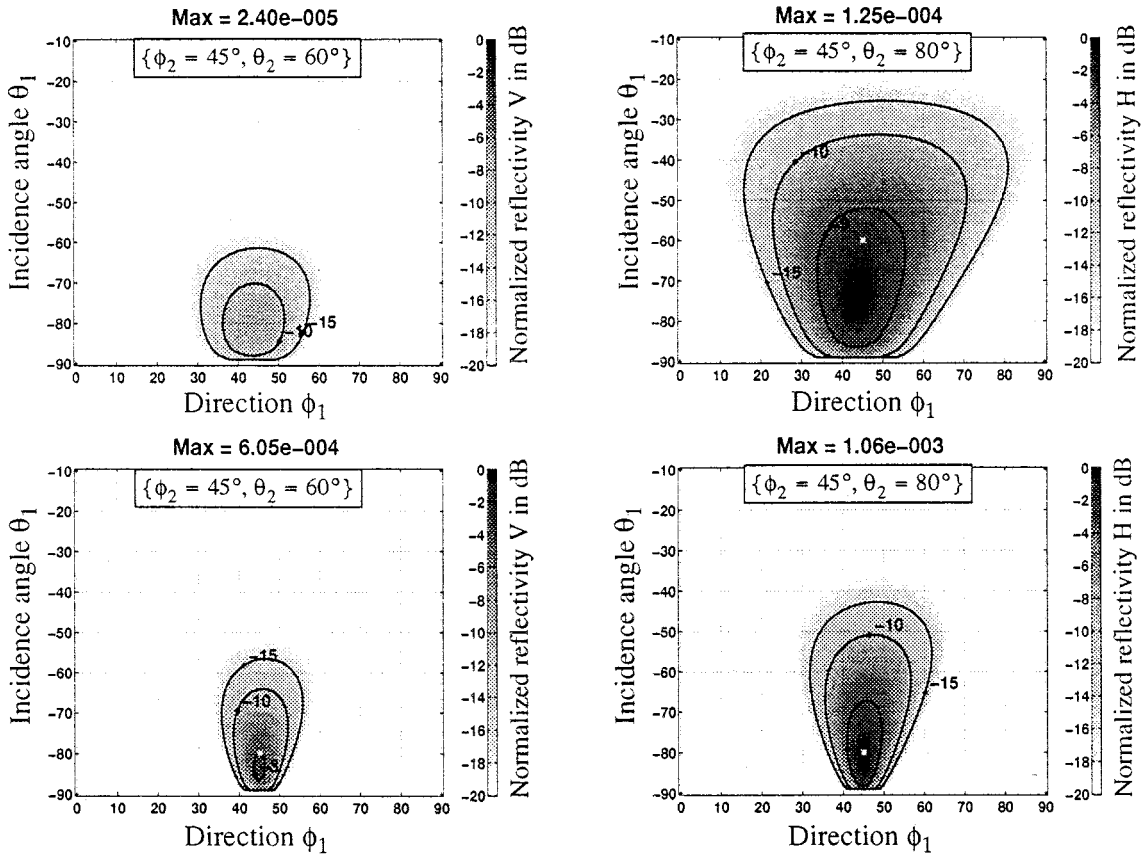

Fig. 8. Normalized reflectivity by Max(w_H) versus the azimuthal direction ϕ_1 according to the wind direction and the incidence angle θ_1 in V and H polarizations with $u_{12} = 10.3$ m/s, $\lambda = 4$ μm, and for an infinite surface.

(18), defined from the sea index n given by Hale and Querry [21] for a temperature equal to 25° C. The wavelength is in the infrared band and near-infrared band at about 0.7 to 100 μm. The attenuation of infrared radiation is frequency and temperature dependent. A number of so-called windows exist in the practical range of infrared radiation frequencies. In these windows, the transmittance of the infrared radiation is high. The windows of practical interest for the infrared optronic systems are at 8 to 13 μm, the 3 to 5 μm window, and the near-infrared window is 0.7 to 2 μm. Between these windows, we find absorption bands mainly due to the presence of water vapor and carbon dioxide. In this paper, we do not study the near infrared band.

In Fig. 7, the average emissivity integrated over $\lambda \in [3; 5]$ μm and $\lambda \in [8; 12]$ μm with an integration step equal to 0.2 μm (this step is sufficient because the sea refraction index varies weakly with the wavelength) is plotted versus the incidence angle θ and the azimuthal direction ϕ according to the wind direction in V and H polarizations with $u_{12} = 10.3$ m/s and an infinite surface. We see that the emissivity is larger in V polarization, decreases with the incidence angle and the direction ϕ, but varies weakly with ϕ. For incidence angles smaller than 30°, the emissivity is equal to a constant, and it is given approximately by the emissivity of a plane with $\theta = 0^o$

$$\varepsilon_V = \varepsilon_H = 1 - \left|\frac{n-1}{n+1}\right|^2 \tag{32}$$

and $\varepsilon_V^{\lambda\in}[3; 5] = 0.97$, $\varepsilon_V^{\lambda\in}[8; 12] = 0.99$. We also observe a slight enhancement of the emissivity to near Brewster's angle defined for $\theta_B = \text{atan}(|n|) = 53°$ in V polarization. As shown in Table I, the variation of the emissivity $\Delta\varepsilon$ is less important with the wind speed and in V polarization.

In Fig. 8, the normalized reflectivity with the maximum at w_H is represented with respect to the azimuthal direction ϕ_1 and the incidence angle θ_1 in V and H polarizations, with $u_{12} = 10.3$ m/s and $\lambda = 4$ μm for an infinite surface. We observe that the reflectivity is maximum around the specular direction given by $\{\phi_1 = \phi_2, \theta_1 = -\theta_2\}$, and the maximum increases with the incidence angle θ_2 with a diminution of lobe width. Since the values of the reflectivity are much smaller than the unity, the multiple reflections are negligible.

In Fig. 9, the average hemispherical reflectivity on $\lambda \in [3; 5]$ μm and $\lambda \in [8; 12]$ μm is plotted as functions of the azimuthal direction ϕ according to the wind direction and the incidence angle θ in V and H polarizations with the same conditions as Fig. 7. It is obtained by integrating the reflectivity over the half-space

$$w_{\text{hem}}(\theta, \phi) = \int_{\theta_1=-(\pi/2)}^{\theta_1=(\pi/2)} d\theta_1 \left[\int_{\phi_1=0}^{\phi_1=\pi} w(\theta_1, \phi_1, \theta_2, \phi_2)\, d\phi_1\right]\Bigg|_{\theta_2=\theta,\, \phi_2=\phi}. \tag{33}$$

Contrary to the emissivity, the hemispherical emissivity increases with the incidence angle. In fact, these two magnitudes are antagonists, and we have approximately the relationship $\varepsilon \approx 1 - w_{\text{hem}}$. Consequently, for grazing angles, the atmospheric ra-

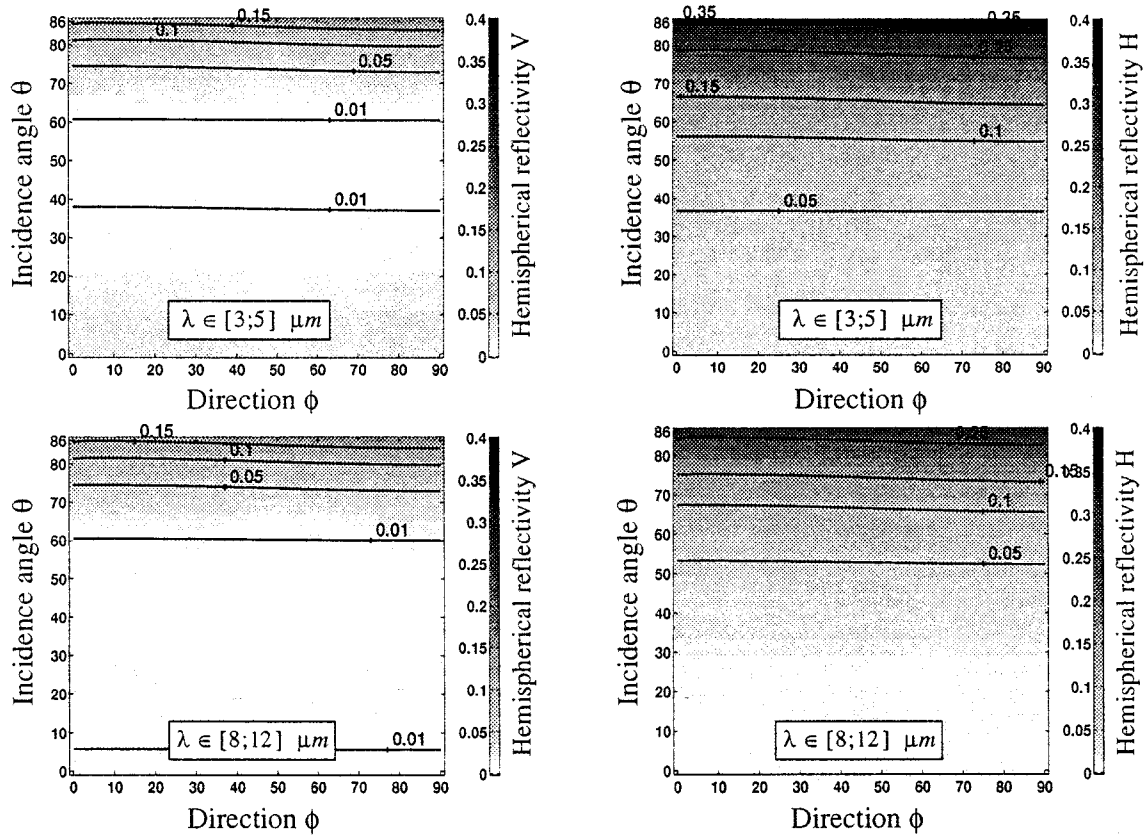

Fig. 9. Average hemispherical reflectivity on $\lambda \in [3;5]\,\mu$m and $\lambda \in [8;12]\,\mu$m versus the azimuthal direction ϕ according to the wind direction and the incidence angle θ in V and H polarizations with $u_{12} = 10.3$ m/s for an infinite surface.

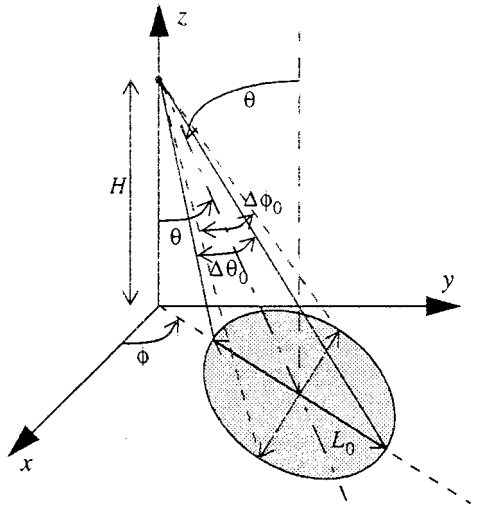

Fig. 10. Determination of the observed surface length L_0.

diation reflected from the sea surface may be affected by the intrinsic radiation of the surface.

Fig. 10 shows that the observation length in ϕ direction is written as

$$L_0 = (H \times \Delta\theta_0)/\cos^2(\theta) \tag{34}$$

where H is the height of the camera of field of view $\Delta\theta_0$, which is of the order mrad. From two-scale model [5], the parameter (12) $L_S = \omega/\sigma_X$ is computed by using a gravity wave characterized by the 2-D spatial autocorrelation function $R_{2d}(l, \phi)$ of the heights modeled as [17, (1.45)]. Hence

$$L_S(\phi, u_{10}) = \frac{\omega}{\sqrt{\dfrac{\partial^2}{\partial l^2}[-R_{2d}(l,\phi)]\Big|_{l=0}}} = \frac{L_C}{\sqrt{2 + \left(\dfrac{L_C}{L'_C}\right)^2 + \dfrac{A}{4}\cos(2\phi)\left(\dfrac{L_C}{L'_2}\right)^2}} \tag{35}$$

where u_{10} is the wind speed at 10 m above the sea. Unlike [1], [2], the parameter [(2b) with $\sigma = \sigma_X$] is determined from (14) Cox and Munk capillary model, whereas they use the JONSWAP gravity spectrum. Substituting (35) and (34) into (12), and using (2b) with $\sigma = \sigma_X$, we obtain

$$v \times y_0 = \frac{2H \times \Delta\theta_0}{L_C} \sqrt{\frac{2 + \left(\dfrac{L_C}{L'_C}\right)^2 + \dfrac{A}{4}\cos(2\phi)\left(\dfrac{L_C}{L'_2}\right)^2}{2[\alpha + \beta\cos(2\phi)]}} \times \frac{1}{\sin(2\theta)}. \tag{36}$$

The product $v * y_0$ is minimum when $\theta = 45°$ and becomes infinite when $\theta = \{0, 90\}°$. For a wind speed $u_{10} = 10$ m/s and $H = 200$ m, we have $L_C = 17.2$ m, $L_S(\phi = \{0°, 90°\}) = \{8.9,$

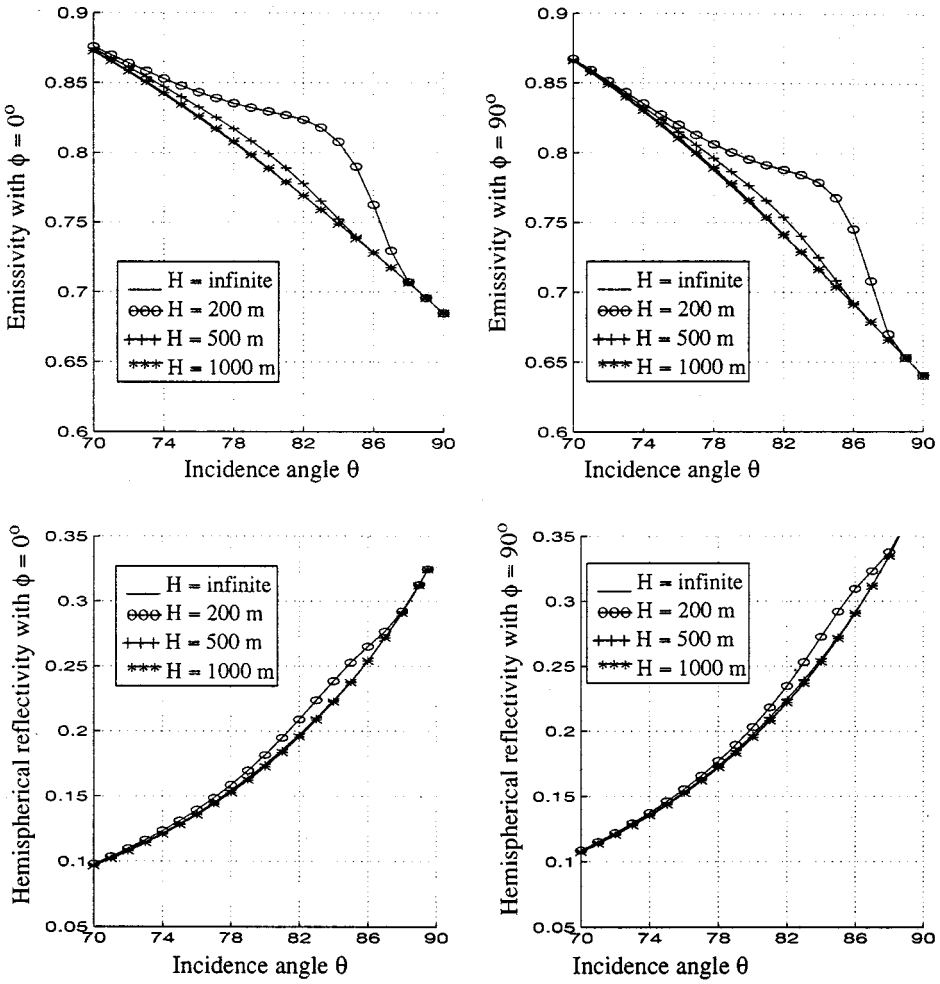

Fig. 11. Unpolarized emissivity and hemispherical reflectivity for $\phi = \{0, 90\}^\circ$ versus the incidence angle θ with $H = \{200, 500, 1000, \text{infinite}\}$ m, $\lambda = 4\,\mu$m and $\Delta\theta_0 = 1$ mrad.

13.2\}m, $H * \Delta\theta_0 = 0.2$ m, and $v * y_0(\phi = \{0°, 90°\}) = \{0.16, 0.13\}/\sin(2\theta)$.

Fig. 11 represents the unpolarized emissivity $(\varepsilon_V + \varepsilon_H)/2$ versus the incidence angle θ, with $\phi = \{0°, 90°\}$, $H = \{200, 500, 1000, \infty\}$ m, $\lambda = 4\,\mu$m, and $\Delta\theta_0 = 1$ mrad. We see that a diminution of the height H, involves an enhancement of the emissivity around $\theta = 80°$, due to the fact that the shadowing function is larger, but the emissivity remains a decreasing function of the incidence angle. Above $H = 1000$ m, the emissivity becomes equal to the emissivity of an infinite surface for any θ. Consequently, the effect of the observation length is notable for grazing angles and at low altitude. Of course, if the field of view $\Delta\theta_0$ increases, the limit height where the effect of the observation length is negligible also increases. Fig. 11 also depicts the hemispherical reflectivity in the same conditions as previous. To note that in the 2-D bistatic case, $v * y_0$ becomes $\{v_1 * y_{01}, v_2 * y_{02}\}$ according to the transmitter and the receiver by replacing $\{\theta = \theta_1, \phi = \phi_1\}$, and $\{\theta = \theta_2, \phi = \phi_2\}$ in (36), respectively.

IV. Sea Surface Apparent Temperature

The radiation incident upon the infrared camera from any specify direction may contain components originating from several different sources (specifically, self-emitted radiation from the surface quantified by the emissivity, self-emitted upward radiation from the atmosphere characterized by the atmospheric transmission coefficient, and downward-emitted atmospheric radiation that is reflected by the surface in the direction of the camera, quantified by the hemispherical reflectivity). Consequently, the surface intrinsic radiation is modified by the presence of the atmosphere. In this calculation, we assume there is no sun reflection on the sea. The optronic imaging is measured by the camera at night. In the previous paragraph, we have shown that the emissivity is much larger than the hemispherical reflectivity for normal incidence angles, but they become of the same order for incidence angles larger than 60°. This paragraph compares the intrinsic sea surface apparent temperature with the one measured by the camera corresponding to the total radiation. Including the atmospheric radiation, the brightness l_{cam} received by the camera obtained from the radiative transfer method is

$$l_{\text{cam}} = \tau_{\text{atm}} \times \varepsilon \times L(\lambda, T_{\text{sur}}) + L(\lambda, T_{\text{atm}}) \times [1 - \tau_{\text{atm}} \times (1 - w_{\text{hem}})] \quad (37)$$

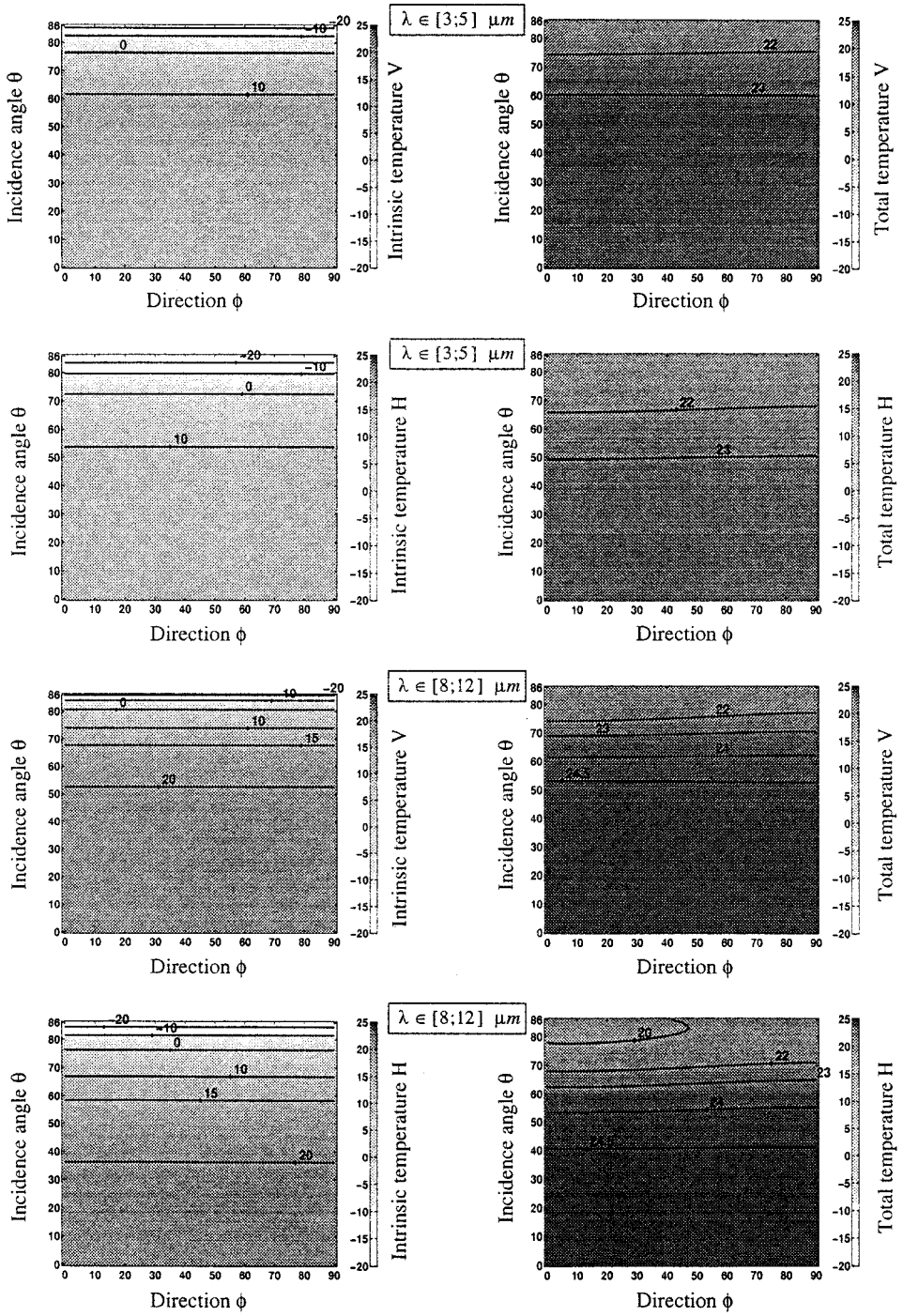

Fig. 12. Intrinsic and total surface average apparent temperatures on $\lambda \in [3;5]$ μm and $\lambda \in [8;12]$ μm versus the azimuthal direction ϕ according to the wind direction and the incidence angle θ in V and H polarizations with $u_{12} = 10.3$ m/s for an infinite surface.

with τ_a the atmospheric coefficient transmission, ε the sea surface emissivity given by (20), $w_{\rm hem}$ the hemispherical emissivity determined by (29), $\{T_{\rm sur}, T_{\rm atm}\}$ the surface and atmospheric temperatures, respectively, and $L(\lambda, T)$ the blackbody radiation given by Planck's law at a wavelength λ and at a temperature T. The first term of (37) corresponds to the surface intrinsic radiation, and the second term is the radiation provided by the atmosphere composed of the reflected radiation and the intrinsic radiation. The surface apparent temperature $T_{\rm app}$ is given by [3, (3.23a)]

$$T_{\rm app} = \frac{C_2}{\lambda} \frac{1}{\ln\left\{\left[\exp\left(\frac{C_2}{\lambda T}\right) - 1 + \varepsilon_S\right] \Big/ \varepsilon_S\right\}} \quad \begin{cases} C_1 = 1.192 \times 10^{-16}\ \text{W.m}^2 \\ C_2 = 1.439 \times 10^{-2}\ \text{m.K.} \end{cases} \tag{38}$$

Since the emissivity is smaller than unity (for a blackbody it is equal to one) the surface apparent temperature $T_{\rm app}$ is always smaller than the surface temperature T. In microwaves regions, $C_2/(\lambda T)$ is much smaller than unity, which involves $T_{\rm app} = \varepsilon_S T$ being a linear function of the emissivity. The sea surface apparent intrinsic temperature $T_{\rm app}^{\rm int}$ within the atmosphere, and the total atmospheric apparent temperature T_{app}^{atm} are calculated from (38), with $\{\varepsilon_S = \tau_{\rm atm}\varepsilon, T = T_{\rm sur}\}$ and $\{\varepsilon_S = 1 - \tau_{\rm atm}(1 - w_{\rm hem}), T = T_{\rm atm}\}$, respectively. (37) becomes

$$l_r = L\left(\lambda, T_{\rm app}^{\rm int}\right) + L\left(\lambda, T_{\rm app}^{\rm atm}\right). \tag{39}$$

Applying (38), we show that the apparent temperature $T_{\rm app}^{\rm cam}$ measured by the camera is

$$T_{\rm app}^{\rm cam} = \frac{C_2}{\lambda}\left[\ln\left\{\frac{\exp\left[\frac{C_2}{\lambda}\left(\frac{1}{T_{\rm app}^{\rm int}} + \frac{1}{T_{\rm app}^{\rm atm}}\right)\right] - 1}{\exp\left(\frac{C_2}{\lambda T_{\rm app}^{int}}\right) + \exp\left(\frac{C_2}{\lambda T_{\rm app}^{\rm atm}}\right) - 2}\right\}\right]. \tag{40}$$

Fig. 12 represents the intrinsic $T_{\rm app}^{\rm int}$ and total $T_{\rm app}^{\rm cam}$ surface average apparent temperatures on $\lambda \in [3; 5]$ μm and $\lambda \in [8; 12]$ μm, with an integration step equal to 0.2 μm, versus the azimuthal direction ϕ and the incidence angle θ , in V and H polarizations with $u_{12} = 10.3$ m/s for an infinite surface. The atmospheric transmission coefficient $\tau_{\rm atm}(h, \lambda)$ along the path of length $h = H/\cos\theta$ is evaluated by the Taylor and Larmor model [4] with the following meteorological conditions: visibility distance equal to 10 km, humidity of the atmosphere equal to 60%, $T_{\rm sur} = 25°$ C, $T_{\rm atm} = 20°$ C, $H = 200$ m. The temperature and the humidity atmosphere are assumed to be uniform, the atmospheric transmission coefficient is assumed to be independent of the incidence angle θ and the direction ϕ, but it is a function of the wavelength λ and the distance h. We can evaluate atmospheric transmission coefficient with Modtran code [22]. As depicted in Fig. 12, the surface intrinsic apparent temperature decreases with the incidence angle and varies very weakly with the direction ϕ. In general, the variations of the apparent temperature is larger in H polarization and in the atmospheric transparence window $\lambda \in [8; 12]$ μm. We see that the atmospheric radiation modified the intrinsic radiation under grazing incidence angles due to the fact that the hemispherical reflectivity is important and that for normal incidence angles the intrinsic radiation remains affected by the atmospheric radiation.

V. Discussion and Conclusion

We have developed a method for correcting the SST by rigorously including the surface emissivity and reflectivity. The method is based on Yoshimori [2] and Bourlier [3] works. Contrary to Yoshimori, our emissivity and reflectivity models use the monostatic and bistatic 2-D shadowing functions instead of those obtained in the 1-D case. In addition, the effect of the observation length is introduced contrary to [3], which determines the 2-D emissivity for an infinite observation length.

The model is valid for a stochastic 2-D surface, which has a mean curvature radius much larger than the wavelength, which allows the application of the geometrical-optics approximation. From a two-scale model, the simulations show that the sea emissivity and the sea hemispherical reflectivity decrease with observation length due to the fact that the illuminated surface ratio also decreases. For the emissivity, an enhancement was observed up to an incidence angle equal to 84°. In fact, if the observation length becomes very small, then this augmentation is larger than the unity, which has no practical meaning. The observation length becomes smaller than the correlation length of the stochastic process. Therefore, the statistics of the stochastic process are not included completely, which means that the surface is described statistically with less accuracy. We note a similar behavior with Wagner's shadowing function. Another explanation is that the Smith and Wagner approaches assumed that the correlation between the slopes and the heights is null, involving that for an infinite observation length, there is an overestimation of the shadowing function [12]. For a finite surface, this overestimation may become more important.

The simulations show that the hemispherical reflectivity and emissivity are antagonistic and their sum is approximately equal to one, similar to the relation provided by a plane. So for normal incidence angles, the emissivity is much larger than the hemispherical reflectivity, which involves the atmospheric radiation reflected by the sea surface being negligible to the sea surface intrinsic radiation (which is proportional to the emissivity). This method may be applied on the satellite systems located at high altitude. Unlike for incidence angles larger than 60° corresponding to observation platforms located at low altitude, the hemispherical reflectivity becomes significant, implying that the radiation reflected by the sea surface must be taken into account with the atmospheric radiation for determining the total SST measured by the infrared camera.

The radiative transfer method allows us to calculate the total STT composed of two terms. The first term gives the sea surface intrinsic radiation obtained from the emissivity. The second term corresponds to the atmospheric radiation quantified by the atmospheric transmission coefficient and the one reflected by the sea surface, characterized by the hemispherical reflectivity. For given meteorological conditions, the atmospheric transmission coefficient is evaluated from the Taylor and Larmor model [4]. We have simulated the total SST and compared it with the intrinsic STT according to the polarization, the wind direction, the incidence angle, and for two atmospheric transparence windows. Other contributions can be added to this model such as sun reflection by the sea, cloud self-emission, etc.

References

[1] K. Yoshimori, K. Itoh, and Y. Ichioka, "Thermal radiative and reflective characteristics of a wind-roughened water surface," *J. Opt. Soc. Amer. A*, vol. 11, no. 6, pp. 1886–1893, June 1994.

[2] ——, "Optical characteristics of a wind-roughened water surface: A two-dimensional theory," *Appl 0pt.*, vol. 34, no. 27, pp. 6236–6247, Sept. 1995.

[3] C. Bourlier, J. Saillard, and G. Berginc, *Emissivity of the Sea Surface*, J. A. Kong, Ed. Cambridge, MA: EMW, 2000, pp. 288–312.

[4] G. Gaussorgues, *La thermographie infrarouge, principes, technologies, applications*. Paris, France: TEC & DOC, 1999.

[5] F. T. Ulaby, R. K. Moore, and A. K. Fung, "Microwave remote sensing," in *Theory to Applications*. New York: Artech House, 1986, vol. I–II.

[6] J. T. Johnson and M. Zang, "Theoretical study of the small slope approximation for ocean polarimetric thermal emission," *IEEE Trans. Geosci. Remote Sensing*, vol. 37, pp. 2305–2316, Sept. 1999.

[7] P. D. Watts, M. R. Allen, and T. J. Nightingale, "Wind speed effects on sea surface emission and reflection for the along track scanning radiometer," *J. Atmos. Ocean. Technol.*, vol. 13, pp. 126–141, Jan. 1996.
[8] K. Masuda, T. Takashima, and Y. Takayama, "Emissivity of pure and sea waters for the model sea surface in the infrared window regions," *Remote Sens. Environ.*, vol. 24, pp. 313–329, 1988.
[9] P. M. Saunders, "Shadowing on the ocean and the existence of the horizon," *J. Geophys. Res.*, vol. 72, pp. 4643–4649, 1967.
[10] X. Wu and W. L. Smith, "Emissivity of rough sea surface for 8–13 μm: Modeling and verification," *Appl. Opt.*, vol. 36, pp. 2609–2619, Apr. 1997.
[11] C. R. Zeiss, C. P. MacGrath, K. M. Littfin, and H. G. Hughes, "Infrared radiance of the wind-ruffled sea," *J. Opt. Soc. Amer. A*, vol. 16, pp. 1439–1452, June 1999.
[12] C. Bourlier, J. Saillard, and G. Berginc, *The Shadowing Function*, J. A. Kong, Ed. Cambridge, MA: EMW, 2000, pp. 226–287.
[13] B. G. Smith, "Lunar surface roughness, shadowing and thermal emission," *J. Geophys. Res.*, vol. 72, pp. 4059–4067, Aug. 1967.
[14] B. G. Smith, "Geometrical shadowing of a random rough surface," *IEEE Trans. Antennas Propagat.*, vol. 15, pp. 668–671, Sept. 1967.
[15] R. J. Wagner, "Shadowing of randomly rough surfaces," *J. Acoust. Soc. Amer.*, vol. 41, no. 1, pp. 138–147, June 1966.
[16] C. S. Cox and W. H. Munk, "Statistics of the sea surface derived from sun glitter," *J. Marine Res.*, vol. 13, pp. 198–226, 1954.
[17] C. Bourlier, J. Saillard, and G. Berginc, *Study of the Sea Behavior*, J. A. Kong, Chief, Ed. Cambridge, MA: EMW, 2000, pp. 193–225.
[18] P. Beckman, "Shadowing of random rough surfaces," *IEEE Trans. Antennas Propagat.*, vol. AP-13, pp. 384–388, May 1965.
[19] L. M. Ricciardi and S. Sato, "On the evaluation of first passage time densities for gaussian processes," *Signal Process.*, vol. 11, pp. 339–357, 1986.
[20] ——, "A note on first passage time problems for gaussian processes and varying boundaries," *IEEE Trans. Inform. Theory*, vol. IT-29, pp. 454–457, May 1983.
[21] G. M. Hale and M. R. Querry, "Optical constants of water in the 200-nm to 200-μm wavelength region," *Appl. Opt.*, vol. 12, pp. 555–563, 1973.
[22] M. S. Longuet Higgins, "Reflection and refraction at a random moving surface I. Pattern and paths of specular points," *J. Opt. Soc. Amer. A*, vol. 50, pp. 838–844, 1960.

Christophe Bourlier was born in La Flèche, France, on July 6, 1971. He received the DEA degree from the University of Rennes, Rennes, France, in 1995, and the Ph.D. degree from the SEI Electronic Systems and Computer Engineering Laboratory, IRESTE, University of Nantes, Nantes, France, in 1999.

He was with the Laboratory of Radiocommunication, University of Nantes, where he worked on antenna coupling in the VHF-HF band. He is currently working on rough surfaces in the infrared band and on the problems of scattering from rough surfaces.

Gèerald Berginc was born in Etain, France, on March 25, 1959. He received the Dipl. Ing. degree from Ecole Nationale Supérieure de Physique, Marseille, France, and the DEA degree in theoretical physics (hons.) from the University Aix-Marseille, in 1983.

From 1985 to 1987, he was with Thomson-CSF, France, where he was a Research Engineer and was involved in the development of radar performance calculation methods. From 1987 to 1990, he was with Mothesim, France, as Head of the Underwater Acoustic Research Department and a Consultant for modeling electromagnetic phenomena radar and space systems. From 1990 to 1991, he was with Thomson-CSF DAS Optronique, where he is currently Leader of a research group in the Research and Development Department. His research activities include diffraction theory , high frequency asymptotics, rough surface and random media scattering, localization effects and frequency selective surfaces. He is author of more than 40 journal articles, conference papers, book chapters, and he holds 20 patents.

He is a member of the Electromagnetics Academy, SPIE, and a URSI correspondent (commisions B and F).

Joseph Saillard was born in Rennes, France, in 1949. He received the Ph.D. degree and the "Docteur d'Etat" in phyics from the University of Rennes, in 1974 and 1984, respectively.

From 1973 to 1988, he was with the University of Rennes as an Assistant and an Assistant Professor. From 1985 to 1987, he worked for the Ministry of Defense (CELAR) on radar signal processing, and is now a Professor at the University of Nantes (EPUN-IRESTE), Nantes, France, and is in charge of the RADAR research team in the SETRA Group, which is associated with with IRCCyN (UMR n° 6597 CNRS). His research interests are radar polarimetry, adaptive antennas, and electronics systems. These activities are done in close collaboration with other public research organizations and industries.

Dr. Saillard is a member of the Electromagnetics Academy, and is also the organizer of JIPR '90, '92, '95, and '98..